NANO LETTERS

Letter

pubs.acs.org/NanoLett

Tethering Luminescent Thermometry and Plasmonics: Light Manipulation to Assess Real-Time Thermal Flow in Nanoarchitectures

Carlos D. S. Brites,[†] Maria Cecilia Fuertes,[‡,§] Paula C. Angelomé,[‡] Eduardo D. Martínez,[‡] Patrícia P. Lima,[†] Galo J. A. A. Soler-Illia,*[,‖] and Luís D. Carlos*[,†]

[†]Departamento de Física and CICECO - Aveiro Institute of Materials, Universidade de Aveiro, Campus Santiago, 3810−193 Aveiro, Portugal

[‡]Gerencia Química, CNEA, CONICET, Avenido Gral. Paz 1499 (B1650KNA) San Martín, Buenos Aires, Argentina

[§]Instituto Sabato, UNSAM, CNEA, Avenido Gral. Paz 1499 (B1650KNA) San Martín, Buenos Aires, Argentina

[‖]INS. UNSAM, CONICET, Avenido 25 de Mayo 1021, San Martín, Buenos Aires, Argentina

Supporting Information

ABSTRACT: The past decade has seen significant progresses in the ability to fabricate new mesoporous thin films with highly controlled pore systems and emerging applications in sensing, electrical and thermal isolation, microfluidics, solar cells engineering, energy storage, and catalysis. Heat management at the micro- and nanoscale is a key issue in most of these applications, requiring a complete thermal characterization of the films that is commonly performed using electrical methods. Here, plasmonic-induced heating (through Au NPs) is combined with Tb^{3+}/Eu^{3+} luminescence thermometry to measure the thermal conductivity of silica and titania mesoporous nanolayers. This innovative method yields values in accord with those measured by the evasive and destructive conventional 3ω-electrical method, simultaneously overcoming their main limitations, for example, a mandatory deposition of additional isolating and metal layers over the films and the previous knowledge of the thermal contact resistance between the heating and the mesoporous layers.

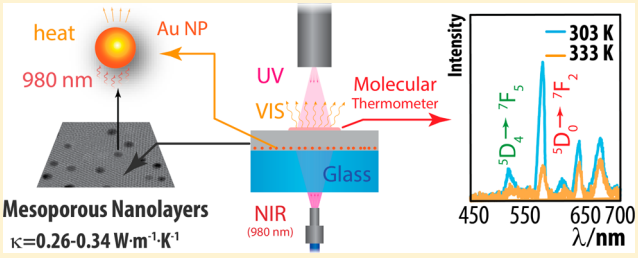

KEYWORDS: *Mesoporous thin films, luminescent molecular thermometry, plasmonic heating, thermal conductivity, gold nanoparticles*

The fabrication of highly integrated nanodevices with a series of interacting components has a profound impact in nanotechnology development, demanding, however, a complete thermal characterization, particularly in applications dealing with on-chip heat management, such as micro- and nanoelectronics, microfluidics, catalysis, thermoelectric energy conversion, and theranostic nanomedicine.[1,2] Further understanding and engineering of nanoscale heat transfer processes are being driven by diverse experimental techniques to accurately measure the thermal dynamics occurring at the submicrometric scale, together with the advancements in computational simulations.[1−7]

The thermal conductivity of thin films (<10^{-6} m) is usually measured by electrical or laser-based methods, analyzing the material's response to a thermal disturbance.[5] In electrical methods, a metal strip (e.g., Al or Si_3N_4), acting simultaneously as heater and thermometer, is deposited on the surface of the material whose thermal conductivity is unknown.[8,9] The 3ω-method is the most used electrical technique employing an alternated heating current and measuring the temperature through the third harmonic of the voltage signal.[5,10,11] A significant contribution from the substrate to the thermal conductivity and the previous knowledge of the thermal contact resistance between the heater/thermometer layer and the thin film are some of the drawbacks of the method.[11,12] In comparison to the 3ω-method, laser-based techniques, as time-domain thermoreflectance,[5] are much less evasive presenting the additional advantage of distinguish the thermal conductivity of the thin film from the thermal conductance of its interfaces.[5,13] On the other hand, complex experimental setup and powerful picosecond laser sources are needed, invalidating the routine implementation of the technique. Noncontact methods to determine the thermal conductivity of solids also include the analysis of the photoluminescence of GaN semiconductors.[14] In this case, however, the relative thermal sensitivity is quite reduced (<0.5%·K^{-1}) resulting, typically, in large temperature uncertainties (5−10 K).

Nanomaterials with controlled porosity present high technological interest because their thermal conductivities can be finely tuned by adjusting the synthesis route. Moreover, as these materials might present a small dielectric constant (low-κ

Received: April 6, 2017
Revised: July 7, 2017
Published: July 7, 2017

DOI: 10.1021/acs.nanolett.7b01433
Nano Lett. XXXX, XXX, XXX−XXX

dielectrics[15]), applications in sensing, electrical and thermal isolation, microfluidics, solar cells engineering, energy storage, and (photo)catalysis are envisaged.[16−19] Mesoporous thin films with highly controlled pore systems, for instance, presents high technological value because they can be combined with optically or catalytically active molecular, polymeric or biological fragments, becoming a highly tunable "nanofacility" in which the well-defined mesopores act as nanocavities with controlled environment, behavior, and positioning.[20] On the other hand, patterning techniques (e.g., scanning probe microscopy and UV or deep X-ray lithography) permits the tailoring of complex structures that exploit the optical, chemical, and catalytic or transport properties at a local scale.[21−23] For these reasons, mesoporous thin films (obtained by spin or dip coating, using the evaporation-induced self-assembly process[24]) are ideal illustrative materials for testing the measurement of the thermal conductivity at the nanoscale.

Luminescence thermometry was reported in the past years as an effective alternative to the conventional electronic-based temperature sensors.[25−30] Although the technique is hastily evolving from the initial breakthrough to real applications,[31] there are still major challenges regarding the conciliation of nanometric probes with high sensitivity and predictability of the thermal response of the system. On the other hand, plasmonic heating permits one to increase the temperature of metallic nanoparticles (NPs) (typically Au or Ag) by means of their irradiation at specific wavelength.[3] The optothermal properties of the plasmonic Au nanostructures can be synthetically tuned, making these particles adequate for controlled heat release applications.[32,33] Here we demonstrate that the combination of light-induced heating with luminescence molecular thermometry constitutes an accurate and precise noncontact technique to infer the thermal conductivity of mesoporous nanolayers.

Two kinds of SiO_2 mesoporous nanolayers were deposited on the top of two different plasmonic heating nanolayers, as schematized in Figure 1. The nanostructures were synthesized using different procedures and the main features are presented in Table 1, (details in the Supporting Information, pages 2−6). Although in route A (samples **1** and **2**), the heating layer is prepared by depositing Au NPs (14.5 ± 1.8 nm) on a glass substrate (Figure 1a−c) in route B (samples **3** and **4**) it is made up of a mesoporous titania (TiO_2) thin film whose pores were partially filled (4%) by Au NPs (7.0 ± 1.0 nm) (Figure 1d,e). The SiO_2 mesoporous layer is deposited on top of the heater layer by dip-coating. Control of the dip-coating withdrawal speed, template removal method, thermal treatment, and templating molecules (cetyltrimethylammonium bromide, CTAB, or triblock copolymer Pluronic F127) leads to adjusting the thickness, pore volume, and pore diameter of the mesoporous SiO_2 layer. The thicknesses and porosities of all the mesoporous layers that form the nanostructures were determined by ellipsometric porosimetry (Supporting Information, pages 7−8).

A luminescent molecular thermometer was deposited on the SiO_2 layer surface exposed to the air (Figure 2a,b) (synthesis and fabrication process in Supporting Information, pages 2−3). The thermometer uses the emission of a Tb^{3+}/Eu^{3+} codoped organic−inorganic diureasil hybrid to infer the surface temperature of each mesoporous structure and was calibrated in the 295−335 K range (Figure 2c). Specifically, the temperature is calculated using the thermometric parameter Δ (Figure 2d) defined by the integrated areas ratio of the $^5D_4 \rightarrow {}^7F_5$ (Tb^{3+}, I_{Tb}) and $^5D_0 \rightarrow {}^7F_2$ (Eu^{3+}, I_{Eu}) transitions:

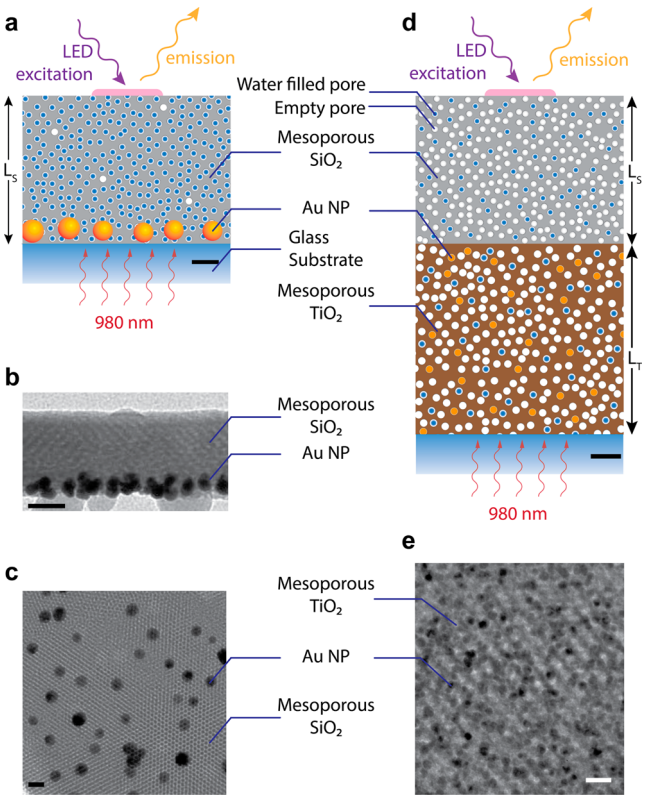

Figure 1. (a) Scaled model of **1** and **2**. (b) Lateral and (c) top view of representative TEM micrographs. (d) Scaled model of **3** and **4**. (e) Top view of a representative TEM micrograph. (Scale bars 20 nm.)

$$\Delta = \frac{I_{Tb}}{I_{Eu}} \quad (1)$$

The relative sensitivity (S_r, eq S3) and the temperature uncertainty (δT) of the molecular thermometer are computed, resulting in a maximum S_r of 7.1 ± 0.2%·K^{-1} and a minimum δT of 0.10 ± 0.02 K, both at 298 K (Figure 2e,f and Supporting Information, pages 9−13). The maximum S_r value is one of the largest reported so far for luminescent thermometers at temperatures around room temperature.[25] The photoluminescence measurements were performed at 50% relative humidity and due to vapor condensation the mesoporous are totally (in **1**) or partially (in the remaining samples) filled with water, as determined by ellipsometry (Table S5 in Supporting Information).

The light-induced heating protocol is a plasmonic process consisting of irradiating the samples across the glass substrate with a 980 nm fiber guided laser that induces a controlled heat release on the metallic NPs embedded into the mesoporous film layers (Figures 2a,b). First, the samples were illuminated during t_0 = 300 s with a given power density and in this steady-state regime, the temperature at the surface of the nanoporous layer exposed to the air was measured using a thermocouple (in contact with the surface) and compared with the value measured by luminescence thermometry, where the integrated areas of the $^5D_4 \rightarrow {}^7F_5$ and $^5D_0 \rightarrow {}^7F_2$ transitions are converted to temperature using the calibration curve shown in Figure 2d. Within the experimental errors of both measurements the two values are similar (Figure S9 in Supporting Information). Subsequently, the 980 nm heating beam is turned off and the emission spectra are recorded in respect to the elapsed time.

DOI: 10.1021/acs.nanolett.7b01433
Nano Lett. XXXX, XXX, XXX−XXX

Table 1. Mesoporous Template, Thickness L (nm), Porosity ϕ (%), and Pore Diameter d (nm) of the SiO_2 (Index S) and TiO_2 (Index T) Layers in 1, 2, 3 and 4

	SiO_2 layer				TiO_2 layer			
sample	template	L_S	ϕ_S	d_S	template	L_T	ϕ_T	d_T
1	SC-E[a,b]	198 ± 5	40 ± 3	2.9 ± 0.2				
2	SF-E[a,b]	106 ± 5	30 + 3	5.6 ± 0.4				
3	SF-C[a,b]	100 ± 8	37 ± 3	6.0 ± 1.0	TF-C[a,b]	145 ± 5	27 ± 3	7.0 ± 0.3
4	SC-C[a,b]	200 ± 10	38 ± 3	6.0 ± 1.0	TF-C[a,b]	145 ± 5	27 ± 3	7.0 ± 0.3

[a]SC, CTAB-templated SiO_2; SF, F127-templated SiO_2; TF, F127-templated TiO_2. [b]-E, extracted template; -C, calcined sample.

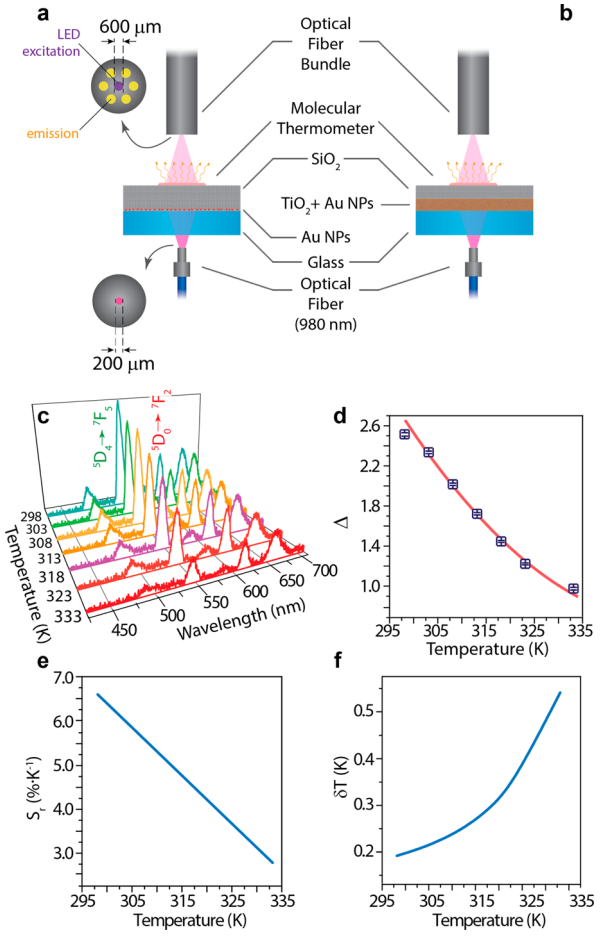

Figure 2. Scheme of the experimental setup used to perform the thermal characterization of (a) **1** and **2** and (b) **3** and **4**. (c) Emission spectra of the molecular thermometer upon 325 nm LED excitation in the 298−333 K range. The Tb^{3+} ($^5D_4 \rightarrow {}^7F_5$) and Eu^{3+} ($^5D_0 \rightarrow {}^7F_2$) transitions used to compute the temperature are identified. (d) Calibration curve of the molecular thermometer. The values reported for the Δ parameter correspond to the average of the thermometric parameter computed from 240 consecutive emission spectra (acquired during 60 s), whereas the error bars are the corresponding standard deviation. The solid line corresponds to the best fit to a second degree polynomial ($r^2 > 0.998$). The temperature is the readout of a K-type thermocouple (0.1 K accuracy). (e) Relative sensitivity and (f) temperature uncertainty of the thermometer in the 298−333 K range.

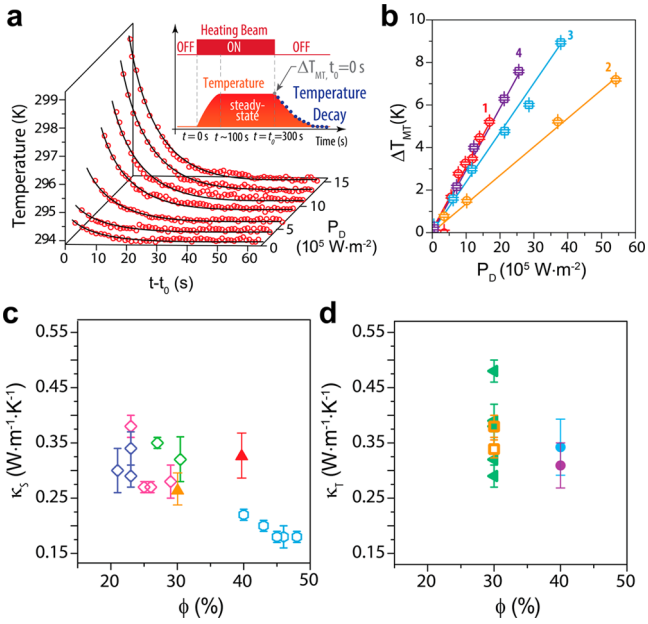

Figure 3. (a) Experimental temperature decay curves of **1**. The dots mark the experimental temperature readout (molecular thermometer) and the lines are fits using eq 2 (Table S2 in Supporting Information). The inset represents schematically the heating protocol. When the 980 nm heating beam is turned on the temperature increases reaching the steady-state regime, $\Delta T_{max} = \Delta T_{MT}$ for $t > 100$ s. Then the laser is turned off and the temperature decay curve is acquired when the sample is cooling until room temperature. (b) Linear dependence of ΔT_{MT} with P_D for **1**, **2**, **3**, and **4**. The solid lines are linear fits with null intercept, the slopes m and the corresponding correlation coefficients r^2 are listed in Table 2 and Table 3. (c) Comparison between the thermal conductivity values calculated for **1** and **2** (red and yellow triangles, respectively) with values of mesoporous SiO_2 thin films with distinct porosities reported in the literature. The values were collected from ref 18 (cubic structure: blue, magenta, and green diamonds stand for B76, P123, and KLE surfactants, respectively. Hexagonal structure: light blue hexagons for P123 surfactant). (d) Comparison between the thermal conductivity values calculated for **3** and **4** (blue and purple circles, respectively) with values of mesoporous TiO_2 thin films with distinct porosities reported in the literature. The values were collected from ref 19 (triangles and squares stand for P123 and KLE surfactants, respectively).

The resulting thermometric parameters are converted to temperature resulting in the cooling curves of Figure 3a and Figure S10 in Supporting Information, well described by the Newton cooling law:[34]

$$T(t) = T_\infty + \Delta T_{max} \exp\left(-\frac{t - t_0}{\tau}\right) \quad (2)$$

where T_∞, ΔT_{max}, t_0, and τ stand for the temperature of the system when $t \rightarrow \infty$ (room temperature), the maximum temperature increase, the time instant when the pump probe is turned off, and the time decay constant, respectively, (Supporting Information, pages 14−16).

DOI: 10.1021/acs.nanolett.7b01433
Nano Lett. XXXX, XXX, XXX−XXX

Table 2. Calculated m ($K{\cdot}m^2{\cdot}W^{-1}$), r^2, $(N_{Au})_S$, N_{wS}, σ_S (m^2), $(\Delta T_{Au}/\Delta T_{MT})_S$, $(\Delta T_w/\Delta T_{MT})_S$, and κ_S ($K{\cdot}m^{-1}{\cdot}W^{-1}$) Values for 1 and 2

sample	m (10^{-6})	r^2	$(N_{Au})_S$ (10^8)	N_{wS} (10^{10})	σ_S (10^{-18})	κ_s	$\left(\frac{\Delta T_{Au}}{\Delta T_{MT}}\right)_S$	$\left(\frac{\Delta T_w}{\Delta T_{MT}}\right)_S$
1	3.20	0.993	1.3	114	0.560	0.33	62.3%	37.7%
2	1.39	0.975	1.3	3	0.437	0.26	93.9%	6.1%

To estimate the thermal conductivity of the mesoporous layers (κ_S for SiO_2 and κ_T for TiO_2) we rationalize the heat transfer processes in the nanostructures based on a one-dimensional lumped elements thermal circuit model.[35−37] The model considers that the Au nanoparticles and the water molecules contained in the pores of the mesoporous layers are independent heat sources and, thus, the total temperature increment is the sum of the temperature increase resulting from each source separately (Figure S11 in Supporting Information). This is exactly the same approximation employed by Swift et al. in the description of the thermal heat flow for power transformers in electronic circuits.[37] The thermal conductivity of the mesoporous thin films is known to be independent of its thickness, as the thermal resistance of the mesoporous films are much higher than the contact resistance.[11,18] Therefore, we consider that the thermal resistances of the mesoporous layers are much higher than the contact resistances. Whereas in **1** and **2** this is justified due to the small contact area between the Au NPs and the SiO_2 layer, in **3** and **4** negligible contact resistances are expected due to the similar nature of the contacting mesoporous layers.

On the other hand, as the thickness of the mesoporous layers (100−200 nm) is much lower than the dimensions of the top and bottom parts of the nanostructures (~4−5 × 10^{-3} m) the heat flow propagates essentially in the same direction of the incident radiation (across the nanolayers thickness) with negligible thermal gradients (10^{-2} K, Supporting Information, page 18).[36] Therefore, the heat dissipation to the surroundings is essentially dominated by the dissipation from the top and bottom surfaces (as the area of the lateral parts is much lower). Moreover, the fraction of the total heating power that is actually going out through the air at the top surface is determined by ρ_j/ρ_g, where ρ_j and ρ_g are the thermal resistances of the mesoporous layers (j = S for SiO_2 or j = T for TiO_2) and the glass substrate, respectively (Figure S11 in Supporting Information).

With these assumptions, and considering moderate temperature increments, the temperature increase at the top surface measured by the molecular thermometer ($\Delta T_{MT} \equiv \Delta T_{max}$) corresponds to

$$\Delta T_{MT} = \frac{\rho_j}{\rho_g}(\Delta T_{Au} + \Delta T_w) = \frac{\rho_j}{\rho_g}\left(\frac{N_{Au}\sigma P_D}{4\pi R\kappa} + \sum_j \frac{4N_{wj}\alpha R_{wj}^2 P_D}{\kappa_j}\right) \quad (3)$$

where ΔT_{Au} and ΔT_w are the temperature increases induced by the laser irradiation of the Au NPs and water molecules contained in the pores of the mesoporous layers, respectively. N_{Au} and N_w stand for the effective number of Au NPs (with radius R) and of pores containing water (with radius R_w) that are releasing heat when illuminated by the 980 nm laser with power density P_D, σ is the absorption cross section of the Au NPs ($Q = \sigma{\cdot}P_D$ represents the heat released per particle),[3,38] and α is the absorption coefficient of water at 980 nm (α = 50.2 m^{-1})[39].

According to this model, ΔT_{MT} is directly proportional to P_D, which is exactly what is observed for all the samples (Figure 3b). Therefore, the thermal conductivities of the SiO_2 layer in **1** (κ_{S1}) and **2** (κ_{S2}) and of the TiO_2 layer in **3** (κ_{T3}) and **4** (κ_{T4}) can be estimated from the corresponding slopes m_i (i = 1−4) of the linear dependences between ΔT_{MT} and P_D, despite the model considers the nanoparticles as a series of independent particles, not taking into account particle−particle interactions. For **1** and **2**, this approximation is reasonable as particle−particle interactions can be indeed negligible, there is practically no superposition between particles (Figure 1c). For **3** and **4**, however, an average particle−particle distance of 10 nm is estimated based on the pore volume, filling fraction, and NP radius. As this interparticle distance is larger than NP size, only a minor plasmon coupling interaction should be considered. Nevertheless, in these systems the deposition of the top silica layer over the gold-loaded mesoporous TiO_2 and the following heating process applied are probably responsible for the differences in the dielectric environment of the particles and the absorption spectra obtained for each sample (Figures S12,13 in Supporting Information). In any case, no significant shift in the plasmon position is detected after thermal treatment, as was reported to occur during heat-induced coalescence of confined particles.[40]

Then, for **1** and **2** the thermal conductivity of the SiO_2 layer is given by

$$\kappa_{Si} = \left[\frac{\kappa_g L_i}{m_i L_g}\left(\frac{(N_{Au})_S\sigma_{Si}}{4\pi R_S} + 4N_{wSi}\alpha R_{wSi}^2\right)\right]^{1/2}, \quad i = 1 \text{ for } \mathbf{1} \text{ and } i = 2 \text{ for } \mathbf{2} \quad (4)$$

where κ_g and L_g are the thermal conductivity and thickness of the glass substrate, respectively, (Supporting Information, page 18), R_S is the center of the size distributions of the Au NPs (Figure S4 in Supporting Information), L_i is the thicknesses of the SiO_2 mesoporous layer, and $R_{wS} = d_S/2$ (Table 1). $(N_{Au})_S$, N_{wS} (effective number of pores containing water in the SiO_2 layer), and σ_S values are listed in Table 2 that also presents the ΔT_{Au} and ΔT_w contributions to the total temperature increment ΔT_{MT}. Whereas the absorption cross sections of the Au NPs at 980 nm are determined numerically by the Mie theory, knowing the index of refraction of the surrounding media and the size of the particles (Table S3 and Figure S2 in Supporting Information), $(N_{Au})_S$ and N_{wS} are estimated based on the effective illuminated volume and on the number of Au NPs and pores filled with water, respectively (details of the calculus in Supporting Information, pages 17−25). The κ_{s1} and κ_{s2} values are then 0.33 ± 0.03 and 0.26 ± 0.04 $W{\cdot}m^{-1}{\cdot}K^{-1}$, respectively (Table 2). Because of the high amount of water within the porous of **1** (Table S5 in Supporting Information), its contribution for the total heating is larger, ~38%, relative to ~6% in **2**, implying, concomitantly, a larger thermal conductivity value.

DOI: 10.1021/acs.nanolett.7b01433
Nano Lett. XXXX, XXX, XXX−XXX

Table 3. Calculated m ($K{\cdot}m^2{\cdot}W^{-1}$), r^2, $(N_{Au})_T$, N_{wT}, σ_T (m^2), $(\Delta T_{Au}/\Delta T_{MT})_T$, $(\Delta T_w/\Delta T_{MT})_T$, and κ_T ($K{\cdot}m^{-1}{\cdot}W^{-1}$) Values for 3 and 4

sample	m (10^{-6})	r^2	$(N_{Au})_T$ (10^8)	N_{wT} (10^9)	σ_T (10^{-18})	κ_T	$\left(\frac{\Delta T_{Au}}{\Delta T_{MT}}\right)_T$	$\left(\frac{\Delta T_w}{\Delta T_{MT}}\right)_T$
3	2.49	0.952	4.6	3.4	0.134	0.34	99.4%	0.6%
4	2.95	0.997	4.6	4.3	0.134	0.31	99.3%	0.7%

The calculated κ_s values are of the same order of magnitude than those listed by Coquil et al.[18] for cubic and hexagonal dehydrated (24 h at 433 K) mesoporous SiO_2 thin films of different porosity (21−48%), 0.18−0.38 $W{\cdot}m^{-1}{\cdot}K^{-1}$. It is well-known that for hydrated samples the thermal conductivity should increase; for instance Bippus et al. noticed a decrease of the thermal conductivity from 0.08 to 0.04 $W{\cdot}m^{-1}{\cdot}K^{-1}$ with the removal of water by thermal treatment in initially water-filled mesoporous SiO_2 particles.[41] Then, the thermal conductivity of **1** and **2** should be larger than the reported values obtained in dehydrated SiO_2 mesoporous samples increasing with the increase on the water content. Figure 3c compares the calculated κ_s values with those measured for similar SiO_2-based mesoporous thin films using the 3ω-method.[18]

The thermal conductivity of the mesoporous TiO_2 layer can be computed using a similar reasoning. When these samples are illuminated by the 980 nm beam, the laser-induced temperature increment measured by the molecular thermometer ΔT_{MT} results from (i) the Au NPs within the pores (with radius R_T) of the TiO_2 layer (ΔT_{Au}); (ii) the water-filled pores (with radius R_{wT}) of the TiO_2 layer (ΔT_{wT}); and (iii) the water-filled pores (with radius R_{wS}) of the SiO_2 (ΔT_{wS}) layer

$$\Delta T_{MT} = \frac{\rho_T}{\rho_g}[\Delta T_{Au} + \Delta T_{wT} + \Delta T_{wS}] = \frac{\rho_T}{\rho_g}\left(\frac{(N_{Au})_T\sigma_T}{4\pi R_T\kappa_T} + \frac{4N_{wT}\alpha R_{wT}^2}{\kappa_T} + \frac{4N_{wS}\alpha R_{wS}^2}{\kappa_S}\right)P_D \quad (5)$$

where R_T is the center of the size distributions of the Au NPs in **3** and **4** (Figure S2 in Supporting Information), $R_{wT} = d_T/2$ (Table 1) and the calculated σ_T, $(N_{Au})_T$ and N_{wT} (effective number of pores containing water in the TiO_2 layer) are listed in Table 3. $(N_{Au})_T$, N_{wT}, and N_{wS} are estimated based on the effective illuminated volume and on the filling percentage of the TiO_2 pores with Au particles (4%) and pores filled with water (Table S5), respectively (details of the calculus in Supporting Information, pages 21−25). With all these values and taken into account the P_D values used in this work (Figure 3b) and the typical thermal conductivity of mesoporous SiO_2 and TiO_2 layers (Figure 3c), eq 5 gives $\Delta T_{MT} \sim 40$ K. As $\Delta T_{MT} < 10$ K (Figure 3b), we may conclude that not all the illuminated Au NPs and water-filled pores contribute for the heating of the mesoporous layers. Thus, to get ΔT_{MT} values consistent with those experimentally measured we consider an effective penetration length for the heating laser beam in the TiO_2 layer corresponding to ∼30% of the total layer thickness (equivalent to the absorption of the laser beam by the six first pore layers). With this assumption, ΔT_{wS} in eq 5 is negligible and the thermal conductivities of the TiO_2 layer in **3** (κ_{T3}) and **4** (κ_{T4}) can be estimated by

$$\kappa_{Ti} = \left[\frac{\kappa_g L_T}{m_i L_g}\left(\frac{(N_{Au})_T\sigma_T}{4\pi R_T} + 4N_{wTi}\alpha R_{wT}^2\right)\right]^{1/2}, \quad i = 3 \text{ for } \mathbf{3} \text{ and } i = 4 \text{ for } \mathbf{4} \quad (6)$$

yielding $\kappa_{T3} = 0.34 \pm 0.05$ $W{\cdot}m^{-1}{\cdot}K^{-1}$ and $\kappa_{T4} = 0.31 \pm 0.04$ $W{\cdot}m^{-1}{\cdot}K^{-1}$ (Table 3). The similarity between these two values is in accord with the analogous structural features of the samples that differ only in the total amount of water within the pores. The table also lists the ΔT_{Au} and ΔT_{wT} contributions to the total temperature increment ΔT_{MT}. Because of the small amount of water within the porous (20−25% of the TiO_2 pores are filled with water, Table S5 in Supporting Information), the contribution of the water in the TiO_2 layer for the total heating is ∼1% (Table 3). The thermal conductivity of **3** and **4** should be also larger than the reported values obtained in dehydrated TiO_2 mesoporous samples, increasing with the increase on the water content. Nevertheless, the obtained values are in agreement with those listed in the literature for amorphous sol−gel dehydrated mesoporous TiO_2 films, 0.25−0.48 $W{\cdot}m^{-1}{\cdot}K^{-1}$.[19,42] Figure 3c compares the values computed in this work with those measured for similar TiO_2-based mesoporous thin films using the 3ω-method.

As an added benefit, our approach enables the measurement of the effective thermal time constant of the system, which permits one to infer the corresponding convective heat transfer coefficient, a characteristic constant that has been difficult to measure by other methods. The value found, ∼140 $W{\cdot}m^{-2}{\cdot}K^{-1}$ (Supporting Information, pages 26−27), is in accord with the values expected for air-forced convection of flat plates.[43] Moreover, we should remark that the measurement of the effective thermal time constant of the system cannot be performed neither by electrical methods nor by infrared thermometry.

In summary, we demonstrated here that light-induced heat releasing from Au NPs embedded into SiO_2 or TiO_2 mesoporous thin films produces controllable temperature increments that can be accurately measured by luminescent thermometry, allowing evaluation of the thermal conductivity of the mesoporous nanolayers. The molecular thermometer uses the emission of a Tb^{3+}/Eu^{3+} codoped organic−inorganic diureasil hybrid presenting a maximum relative sensitivity of 7.1 ± 0.2%·K^{-1} and a minimum temperature uncertainty of 0.10 ± 0.02 K, both at 298 K. The thermal conductivity values obtained by luminescent thermometry, 0.26−0.33 for SiO_2 and 0.31−0.34 $W{\cdot}m^{-1}{\cdot}K^{-1}$ for TiO_2, are in accord with those reported using the conventional and evasive 3ω-electrical method for analogous samples. The method predicts the thermal conductivity of mesoporous thin films, independently of its electrical properties, and is simpler in terms of experimental requirements, because it is uses conventional light sources and portable spectrometers to infer the temperature changes on the samples. Moreover, it overcomes the main limitations of the 3ω electrical method: (i) a mandatory deposition of additional isolating and metal layers over the films

DOI: 10.1021/acs.nanolett.7b01433
Nano Lett. XXXX, XXX, XXX−XXX

and (ii) the previous knowledge of the thermal contact resistance between the heating and the mesoporous layers.

The fruitful combination of luminescent thermometry and plasmonic heating enables the real-time monitoring of the heat fluxes in multilayer devices, helping to unveil their thermal properties. The precise position-sensitive temperature measurements presented here give the design principles that will permit the production of tunable light-triggered heating systems for nanoscale fluidics, electronics, and mechanics. The possibility of this time-space thermal flow assessment permits one to envisage the advanced design of nanoheating architectures with highly controlled thermal flow with applications in light or thermal responsive systems, drug delivery, and molecular sorting.

■ ASSOCIATED CONTENT

Supporting Information

The Supporting Information is available free of charge on the ACS Publications website at DOI: 10.1021/acs.nanolett.7b01433.

Synthesis, experimental details and characterization techniques, photoluminescence, thermal performance characterization, thermal circuit models, Au NPs absorbance and absorption cross section, plasmonic heating, convective heat transfer coefficient, error analysis (PDF)

■ AUTHOR INFORMATION

Corresponding Authors

*E-mail: gsoler-illia@unsam.edu.ar.
*E-mail: lcarlos@ua.pt.

ORCID

Eduardo D. Martínez: 0000-0002-5834-4389
Galo J. A. A. Soler-Illia: 0000-0001-9984-3806
Luís D. Carlos: 0000-0003-4747-6535

Notes

The authors declare no competing financial interest.

■ ACKNOWLEDGMENTS

Financial support of Fundação para a Ciência e a Tecnologia (FCT, Portugal) (PTDC/CTM-NAN/4647/2014 and POCI-01-0145-FEDER-016687) is acknowledged. This work was developed within the scope of the project CICECO-Aveiro Institute of Materials, POCI-01-0145-FEDER-007679 (FCT, UID/CTM/50011/2013), financed by Portuguese funds through FCT/MEC (Ministério da Educação e Ciência) and when appropriate cofinanced by FEDER under the PT2020 Partnership Agreement. Funding was also provided by Argentina agencies CONICET (PIP00044CO) and ANPCyT (PICT 2012-2087). C.D.S.B. (SFRH/BPD/89003/2012) and E.D.M. thank FCT and CONICET, respectively, for the postdoctoral grants. The authors acknowledge the help of Ricardo Longo (UFPE, Recife, Brazil) and Pedro Paulo (IST-UL, Portugal) with the calculus of the absorption coefficient of Au NPs.

■ REFERENCES

(1) Luo, T.; Chen, G. *Phys. Chem. Chem. Phys.* **2013**, *15*, 3389−3412.
(2) Cahill, D. G.; Braun, P. V.; Chen, G.; Clarke, D. R.; Fan, S. H.; Goodson, K. E.; Keblinski, P.; King, W. P.; Mahan, G. D.; Majumdar, A.; Maris, H. J.; Phillpot, S. R.; Pop, E.; Shi, L. *Appl. Phys. Rev.* **2014**, *1*, 011305.
(3) Baffou, G.; Quidant, R. *Laser Photonics Rev.* **2013**, *7*, 171−187.
(4) Pernot, G.; Stoffel, M.; Savic, I.; Pezzoli, F.; Chen, P.; Savelli, G.; Jacquot, A.; Schumann, J.; Denker, U.; Monch, I.; Deneke, C.; Schmidt, O. G.; Rampnoux, J. M.; Wang, S.; Plissonnier, M.; Rastelli, A.; Dilhaire, S.; Mingo, N. *Nat. Mater.* **2010**, *9*, 491−495.
(5) Cahill, D. G.; Ford, W. K.; Goodson, K. E.; Mahan, G. D.; Majumdar, A.; Maris, H. J.; Merlin, R.; Phillpot, S. R. *J. Appl. Phys.* **2003**, *93*, 793−818.
(6) Shi, L.; Dames, C.; Lukes, J. R.; Reddy, P.; Duda, J.; Cahill, D. G.; Lee, J.; Marconnet, A.; Goodson, K. E.; Bahk, J. H.; Shakouri, A.; Prasher, R. S.; Felts, J.; King, W. P.; Han, B.; Bischof, J. C. *Nanoscale Microscale Thermophys. Eng.* **2015**, *19*, 127−165.
(7) Sun, Y. F.; Gao, S.; Lei, F. C.; Xiao, C.; Xie, Y. *Acc. Chem. Res.* **2015**, *48*, 3−12.
(8) Goodson, K. E.; Flik, M. I. *Appl. Mech. Rev.* **1994**, *47*, 101−112.
(9) Goodson, K. E.; Ju, Y. S. *Annu. Rev. Mater. Sci.* **1999**, *29*, 261−293.
(10) Cahill, D. G. *Rev. Sci. Instrum.* **1990**, *61*, 802−808.
(11) Dames, C. Measuring the thermal conductivity of thin films: 3ω and related electrothermal methods. *Annu. Rev. Heat Transfer* **2013**, *16*, 7−49.
(12) Koh, Y. K.; Cahill, D. G. *Phys. Rev. B: Condens. Matter Mater. Phys.* **2007**, *76*, 075207.
(13) Hwang, G.; Kwon, O. *Nanoscale* **2016**, *8*, 5280−5290.
(14) Westover, T.; Jones, R.; Huang, J. Y.; Wang, G.; Lai, E.; Talin, A. A. *Nano Lett.* **2009**, *9*, 257−263.
(15) Miller, R. D. *Science* **1999**, *286*, 421−423.
(16) Innocenzi, P.; Malfatti, L. *Chem. Soc. Rev.* **2013**, *42*, 4198−4216.
(17) Volksen, W.; Miller, R. D.; Dubois, G. *Chem. Rev.* **2010**, *110*, 56−110.
(18) Coquil, T.; Richman, E. K.; Hutchinson, N. J.; Tolbert, S. H.; Pilon, L. *J. Appl. Phys.* **2009**, *106*, 034910.
(19) Coquil, T.; Reitz, C.; Brezesinski, T.; Nemanick, E. J.; Tolbert, S. H.; Pilon, L. *J. Phys. Chem. C* **2010**, *114*, 12451−12458.
(20) Soler-Illia, G. J. A. A.; Angelomé, P. C.; Fuertes, M. C.; Calvo, A.; Wolosiuk, A.; Zelcer, A.; Bellino, M. G.; Martínez, E. D. *J. Sol-Gel Sci. Technol.* **2011**, *57*, 299−312.
(21) Martínez, E. D.; Bellino, M. G.; Soler-Illia, G. J. A. A. *ACS Appl. Mater. Interfaces* **2009**, *1*, 746−749.
(22) Faustini, M.; Marmiroli, B.; Malfatti, L.; Louis, B.; Krins, N.; Falcaro, P.; Grenci, G.; Laberty-Robert, C.; Amenitsch, H.; Innocenzi, P.; Grosso, D. *J. Mater. Chem.* **2011**, *21*, 3597−3603.
(23) Innocenzi, P.; Malfatti, L.; Soler-Illia, G. J. A. A. *Chem. Mater.* **2011**, *23*, 2501−2509.
(24) Brinker, C. J.; Lu, Y.; Sellinger, A.; Fan, H. *Adv. Mater.* **1999**, *11*, 579−585.
(25) Brites, C. D. S.; Millán, A.; Carlos, L. D. Lanthanides in Luminescent Thermometry. In *Handbook on the Physics and Chemistry of Rare Earths*; Bünzli, J.-C. G., Pecharsky, V. K., Eds.; Elsevier Science, B. V.: Amsterdam, 2016; Vol. *49*, pp 339−427.
(26) Brites, C. D. S.; Lima, P. P.; Silva, N. J. O.; Millán, A.; Amaral, V. S.; Palacio, F.; Carlos, L. D. *Adv. Mater.* **2010**, *22*, 4499−4504.
(27) Carlos, L.; Palacio, F. *Thermometry at the Nanoscale: Techniques and Selected Applications*; Royal Society of Chemistry, 2015.
(28) Jaque, D.; Vetrone, F. *Nanoscale* **2012**, *4*, 4301−4326.
(29) Marciniak, Ł.; Bednarkiewicz, A.; Kowalska, D.; Strek, W. *J. Mater. Chem. C* **2016**, *4*, 5559−5563.
(30) Dramićanin, M. D. *Methods Appl. Fluoresc.* **2016**, *4*, 042001.
(31) Brites, C. D.; Xie, X.; Debasu, M. L.; Qin, X.; Chen, R.; Huang, W.; Rocha, J.; Liu, X.; Carlos, L. D. *Nat. Nanotechnol.* **2016**, *11*, 851−856.
(32) Huang, X.; Jain, P. K.; El-Sayed, I. H.; El-Sayed, M. A. *Lasers Med. Sci.* **2008**, *23*, 217−228.
(33) Dreaden, E. C.; Alkilany, A. M.; Huang, X. H.; Murphy, C. J.; El-Sayed, M. A. *Chem. Soc. Rev.* **2012**, *41*, 2740−2779.
(34) Bergman, T. L.; Lavine, A. S.; Incropera, F. P.; DeWitt, D. P. *Fundamentals of Heat and Mass Transfer*, 7th ed.; Wiley: New York, 2011.
(35) Chen, Q.; Ren, J. *Chin. Sci. Bull.* **2008**, *53*, 3753−3761.

DOI: 10.1021/acs.nanolett.7b01433
Nano Lett. XXXX, XXX, XXX−XXX

(36) Lienhard, J. H. *A heat transfer textbook*; Courier Corporation, 2013.
(37) Swift, G.; Molinski, T. S.; Lehn, W. *IEEE Trans. Power Delivery* **2001**, *16*, 171−175.
(38) Lalisse, A.; Tessier, G.; Plain, J.; Baffou, G. *J. Phys. Chem. C* **2015**, *119*, 25518−25528.
(39) Palmer, K. F.; Williams, D. *J. Opt. Soc. Am.* **1974**, *64*, 1107−1110.
(40) Martínez, E. D.; Boissière, C.; Grosso, D.; Sanchez, C.; Troiani, H.; Soler-Illia, G. J. A. A. *J. Phys. Chem. C* **2014**, *118*, 13137−13151.
(41) Bippus, L.; Jaber, M.; Lebeau, B.; Schleich, D.; Scudeller, Y. *Microporous Mesoporous Mater.* **2014**, *190*, 109−116.
(42) Fang, J.; Reitz, C.; Brezesinski, T.; Nemanick, E. J.; Kang, C. B.; Tolbert, S. H.; Pilon, L. *J. Phys. Chem. C* **2011**, *115*, 14606−14614.
(43) Sunil, S. *Int. J. Eng. Res. Technol.* **2015**, *4*, 2−7.

DOI: 10.1021/acs.nanolett.7b01433
Nano Lett. XXXX, XXX, XXX−XXX